Computer Physics Communications 238 (2019) 77–87

Contents lists available at ScienceDirect

Computer Physics Communications

journal homepage: www.elsevier.com/locate/cpc

The finite-element time-domain method for elastic band-structure calculations

Alejandro Cebrecos [a], Dimitri Krattiger [b], Victor J. Sánchez-Morcillo [c], Vicent Romero-García [d], Mahmoud I. Hussein [b,*]

[a] Instituto de Instrumentación para Imagen Molecular, Consejo Superior de Investigaciones Científicas (CSIC), Universitat Politécnica de Valéncia, Camino de Vera S/N, 46085, Valencia, Spain
[b] Ann and H.J. Smead Department of Aerospace Engineering, University of Colorado Boulder, Boulder, CO 80309, USA
[c] Instituto de Investigación para la Gestión Integrada de Zonas Costeras, Universidad Politécnica de Valencia, 46730 Grao de Gandia, Valencia, Spain
[d] Laboratoire d'Acoustique de l'Université du Mans, LAUM UMR 6613 CNRS, Le Mans Université, Avenue Olivier Messiaen, 72085 Le Mans Cedex 9, France

ARTICLE INFO

Article history:
Received 3 October 2017
Received in revised form 19 December 2018
Accepted 21 December 2018
Available online 3 January 2019

Keywords:
Band structure
Dispersion curves
Phononic crystals
Elastic metamaterials
Finite-element time-domain
Finite-difference time-domain

ABSTRACT

The finite-element time-domain method for elastic band-structure calculations is presented in this paper. The method is based on discretizing the appropriate equations of motion by finite elements, applying Bloch boundary conditions to reduce the analysis to a single unit cell, and conducting a simulation using a standard time-integration scheme. The unit cell is excited by a wide-band frequency signal designed to enable a large number of modes to be identified from the time-history response. By spanning the desired wave-vector space within the Brillouin zone, the band structure is then robustly generated. Bloch mode shapes are computed using the well-known concept of modal analysis, especially as implemented in an experimental setting. The performance of the method is analyzed in terms of accuracy, convergence, and computation time, and is compared to the finite-difference time-domain method as well as to a direct finite-element (FE) solution of the corresponding eigenvalue problem. The proposed method is advantageous over FD-based methods for unit cells with complex geometries, and over direct FE in situations where the formulation of an eigenvalue problem is not straightforward. For example, the new method makes it possible to accurately solve a time-dependent Bloch problem, such as the case of a complex unit cell model of a topological insulator where an internal fluid flow or other externally controlled physical fields are present.

1. Introduction

Photonic and phononic crystals emerged in the late 1980's and early 1990's as artificial material systems designed to control electromagnetic [1,2] and mechanical [3,4] wave propagation, respectively, and have attracted intensive research interest ever since. The band structure is a key diagram for describing the wave dispersion characteristics of these periodic materials as it represents the relationship between wave vector and frequency. A band structure is obtained utilizing Bloch's theorem [5,6], which allows the calculations to be performed over only a single unit cell. A significant effort has been made over the last few decades in the development of techniques for band-structure calculations. These include plane-wave expansion (PWE) [3,4,7–12], the transfer-matrix (TM) method [13], multiple scattering theory (MST) [14–18], the finite-element (FE) method [19–22], the finite-difference (FD) method [23–25], and the finite-difference time-domain (FDTD) method [26–31], among others [32–36]. Reviews of periodic materials and band-structure calculations methods can be found in Ref. [37] and Ref. [38] for photonic and phononic crystals, respectively.

Most of these methods are based on steady-state analysis (i.e., harmonic time dependence). The dispersion relation of a periodic system is obtained after solving an eigenvalue problem for wave vectors in the Brillouin zone (BZ) [39]. Among these methods, PWE has been extensively used for acoustic and elastic composites [3,4,12] and it is appropriate for solid–solid and fluid–fluid compositions, while FD methods are more suited for phononic material systems composed of multiple states (e.g., solid–fluid) [25]. However, both methods are not suitable when dealing with irregularly shaped scatterers. Other approaches, such as MST, reported in Refs. [16–18] and numerous subsequent studies for phononic systems, are widely used. The MST method can handle multiple media states, such as elastic scatterers in a fluid or air holes in an elastic solid medium, and can accurately analyze high-contrast problems where other methods (PWE, FD, FE) may exhibit slow convergence. Nevertheless, the geometry of the scatterer is also highly restricted to simple shapes and/or topologies such as media composed usually of cylindrical/spherical scatterers in a host

* Corresponding author.
E-mail address: mih@colorado.edu (M.I. Hussein).

https://doi.org/10.1016/j.cpc.2018.12.016
0010-4655/

medium. Ultimately, FE has been employed as an efficient method for band-structure calculations for phononic material systems by formulating an eigenvalue problem constrained by the application of Bloch boundary conditions. In the context of FE methods, an alternative approach to the usual implementation of Bloch boundary conditions (see Ref. [40] for implementation details) is based on considering a Bloch operator transformation of the governing differential equations to obtain the strong form of the Bloch eigenvalue problem [22]. A major advantage of FE over the previous methods is its ease in handling complex unit-cell geometries, e.g., a unit cell with an irregular distribution of two material phases.

While the PWE, MST, FD, and FE methods assume harmonic time dependence to solve the governing elastic wave equation, some authors have implemented band-structure calculations by computing the time-domain response. Specifically, the FDTD method, where the governing equation is discretized in both space and time, falls into this category. In an earlier version of the method, the computational domain has to include numerous unit cells with an appropriate choice of boundary conditions [25]. By varying the source's excitation frequency, the dependence of attenuation (due to evanescence) with the frequency is obtained and used to identify the band gaps. Following this approach (i.e., using several unit cells), the band structure is computed by analyzing phase differences at the input and the output of a finite-size structure [41,42]. In contrast, Tanaka et al. [29] presented an FDTD approach for phononic material systems in which Bloch boundary conditions are imposed—thus reducing the simulation domain to only a single unit cell— and the band structure is hence computed by varying the wave vector through the BZ using a series of Fourier transforms of the time-history data.

The computational effort associated with band-structure calculations is usually high because it involves solving an eigenvalue problem, in the case of harmonic time dependence, or integrating over a large number of time steps, in the case of time-domain methods. Moreover, this process is done numerous times as the value of the wave vector $\mathbf{k}$ is varied along the BZ [or the Irreducible BZ (IBZ)]. The size of the problem, and hence the computational load, is particularly high when the unit-cell configuration requires a large number of degrees of freedom (DOF) to be properly represented. This could be due to a complex unit-cell material phase topology requiring a finely resolved description. Another case is when the presence of defects is incorporated in the calculations. Defects are known to have a physical influence extending over relatively long ranges in space. This, in turn, necessitates choosing correspondingly large unit cells, known as supercells, for the band-structure calculations. Consequently, large cells imply large numbers of DOF. Iterative eigenvalue solvers exhibit leading-order complexity between $\mathcal{O}(n^2)$ and $\mathcal{O}(n^3)$ for full matrices and approximately $\mathcal{O}(n)$ for sparse matrices, where n is the matrix size. In time-domain algorithms, matrix inversion represents the bottle-neck in terms of the computational effort. The computational complexity of eigenvalue problems is usually higher than matrix inversion for full matrices and, as it will be demonstrated here, of similar order, i.e., $\mathcal{O}(n)$, if a sparse representation of the matrices is employed.

In this paper, we present a new technique which we refer to as the *finite-element time-domain* (FETD) method for elastic band-structure calculations, which may be applied to phononic crystals or periodic elastic materials in general. This technique is analogous to the FDTD method for band structure calculations, although the two numerical methods are inherently different with important implications concerning accuracy, convergence, and speed of computation, as shown in this work.[1] The proposed method is implemented on a one-dimensional (1D) model for longitudinal wave propagation and a two-dimensional (2D) plane-strain model of a phononic crystal that accounts for coupled in-plane longitudinal and shear-vertical wave propagation modes. Consistent mass matrices are used in both the 1D and 2D models, and lumped-parameter mass matrices are also considered in the 2D models. Band-structure calculations are performed incorporating Bloch boundary conditions so that the spatial discretization of the domain is reduced to a single unit cell. The performance of the method is analyzed by computing the elastic band structures for 1D and 2D examples and Bloch mode shapes for the 2D case. The 1D example is a periodic rod formed by an alternation of layers of aluminum and a thermoplastic polymer, namely Acrylonitrile butadiene styrene (ABS). In 2D, two contrasting geometries are presented, both composed of an ABS matrix with an aluminum inclusion located at the center of the unit cell. The first geometry comprises a simple square inclusion and the second has an inclusion featuring a complex shape with varying surface curvatures. Results are compared to those obtained by solving the corresponding standard eigenvalue problem using the FE method, as well as a FDTD method that follows the technique proposed in [29]. The FE method is chosen as the prime reference method for evaluating the accuracy, convergence, and computational efficiency of the proposed FETD method. Compared to the FDTD method, the FETD method represents a favorable alternative because it reduces significantly the errors and provides a much faster convergence rate. Due to the meshing procedure of FE-based formulations, FETD offers a more effective way to dealing with complex geometries. A key advantage of FETD and FDTD, compared to other methods, is that they are more amenable to handling problems for which an eigenvalue formulation is challenging or in some cases even impossible; for example, a multiphysical problem involving a dynamically changing field coupled to the solid medium.

The paper is organized as follows. Section 2 overviews the governing equations and the finite-element modeling framework for Bloch analysis of a unit cell representing the periodic medium. Section 3 covers all the details pertaining to the time simulations and post-processing aspects of the proposed method. Numerical examples and an examination of the performance of the method are provided in Sections 4 and 5, respectively. Finally, the conclusions are summarized in Section 6.

2. Unit-cell finite-element model

The continuum equation of motion for a heterogeneous medium is

$$\nabla \cdot \boldsymbol{\sigma} = \rho \ddot{\mathbf{u}}, \tag{1}$$

where $\boldsymbol{\sigma}$ is the stress tensor, $\mathbf{u}$ is a vector representing the displacement field, ρ is the density and the dot indicates differentiation with respect to time. For an elastic medium,

$$\boldsymbol{\sigma} = \mathbf{C} : \nabla^S \mathbf{u}, \tag{2}$$

where $\mathbf{C}$ is the elasticity tensor, the double dot represents the double-dot product of two tensors, and ∇^S denotes the symmetric gradient operator,

$$\nabla^S \mathbf{u} = \frac{1}{2}\left(\nabla \mathbf{u} + (\nabla \mathbf{u})^T\right). \tag{3}$$

All parameters and field variables are in general space dependent. Substituting Eq. (2) into Eq. (1) the strong form of the general elastodynamic problem is obtained,

$$\nabla \cdot \mathbf{C} : \nabla^S \mathbf{u} = \rho \ddot{\mathbf{u}}. \tag{4}$$

[1] The combination of finite difference or finite elements and time integration is widely used in the literature for a wide range of problems (e.g., see Ref. [43]). In this paper, FDTD and FETD are used only for band-structure calculations of periodic media following Bloch's theorem.

Finite-element discretization. Here we consider the FE method for the spatial discretization of the problem. The solution domain Ω is defined over the unit cell of a 2D lattice spanning the range $0 \leq (x, y) \leq a$, where a is the lattice constant. The strong form of the general elastodynamic problem in Eq. (4) is converted into the weak form by introducing a weighting function $\mathbf{w}$ and integrating over the solution domain [44],

$$-\int_{\Omega} \left(\nabla^{\mathrm{S}}\mathbf{w} : \mathbf{C} : \nabla^{\mathrm{S}}\mathbf{u}\right) d\Omega = \int_{\Omega} \left(\rho\mathbf{w} \cdot \ddot{\mathbf{u}}\right) d\Omega. \tag{5}$$

Note that a force term is not included as we seek to obtain the band structure, and in the case of time simulations the loading is introduced in terms of prescribed displacement. The solution domain is discretized into n_{el} element domains Ω^{e},

$$\Omega = \bigcup_{e=1}^{n_{\mathrm{el}}} \Omega^{\mathrm{e}}. \tag{6}$$

A typical weighting function for an element in the domain has the form

$$\mathbf{w}_1 = N_A \mathbf{w}_{1A}, \quad A = 1, \ldots, n_{\mathrm{en}}, \tag{7}$$

where N_A is a shape function associated with node A, $\mathbf{w}_{1A}$ is the A^{th} component of the approximate weighting function, and n_{en} is the number of element nodes. The time-dependent displacement field is discretized in a similar way,

$$\mathbf{u} = N_B \mathbf{d}_{1B}, \quad B = 1, \ldots, n_{\mathrm{en}}, \tag{8}$$

where $\mathbf{d}_{1B}$ is time dependent and expresses the nodal displacement. Substituting Eq. (7) and Eq. (8) into Eq. (5) yields

$$-\int_{\Omega} \left(\nabla^{S} N_A \mathbf{w}_{1A} : C : \nabla^{S} N_B \mathbf{d}_{1B}\right) d\Omega = \int_{\Omega} \left(\rho N_A \mathbf{w}_{1A} \cdot N_B \ddot{\mathbf{d}}_{1B}\right) d\Omega. \tag{9}$$

Eq. (9) can be expressed as a system of algebraic equations in the following matrix form:

$$\mathbf{M}\ddot{\mathbf{U}} + \mathbf{K}\mathbf{U} = 0, \tag{10}$$

where $\mathbf{M}$ and $\mathbf{K}$ are the mass and stiffness matrices, respectively, and $\mathbf{U}$ and $\ddot{\mathbf{U}}$ are the nodal displacement and acceleration vectors, respectively. The mass and stiffness matrices are assembled from the element-level mass, $\mathbf{M}^{\mathrm{e}}$, and stiffness, $\mathbf{K}^{\mathrm{e}}$, contributions following the direct stiffness method [44],

$$\mathbf{M} = \sum_{\mathrm{e}=1}^{n_{\mathrm{el}}} \mathbf{M}^{\mathrm{e}}, \tag{11}$$

$$\mathbf{K} = \sum_{\mathrm{e}=1}^{n_{\mathrm{el}}} \mathbf{K}^{\mathrm{e}}. \tag{12}$$

Evaluating the integral on the right-hand side of Eq. (9) yields the consistent mass matrix. A disadvantage of the consistent mass formulation is that it generally results in non-zero off-diagonal terms in the mass matrix. This makes the time evolution of Eq. (10) computationally demanding because it requires solution of a system of equations at each time step. Lumped-mass matrices, which are diagonal by construction, offer a more efficient alternative as they enable faster time integrations. There are numerous ways to obtain a lumped mass matrix, but one of the most common is the HRZ method [45]. In the HRZ method, only the diagonal entries of the consistent mass matrix are computed but are scaled such that the total translational mass is preserved in each direction.

The time-evolving elastodynamic wave propagation response is obtained by integration of Eq. (10) in time. Together with the application of periodic Bloch boundary conditions and a proper transient excitation in the form of prescribed displacement, this equation can be solved for different values of the Bloch vector $\mathbf{k}$ to obtain the band structure of a periodic system following the procedure we describe in this paper.

Bloch boundary conditions. Bloch's theorem describes the behavior of a wave in an infinite periodic medium in terms of a wave function in the reciprocal space [6]. In terms of displacement vectors, the theorem takes the form

$$\mathbf{u}\left(\mathbf{x}, \mathbf{k}; t\right) = \tilde{\mathbf{u}}\left(\mathbf{x}, \mathbf{k}\right) e^{\mathrm{i}(\mathbf{k}^{\mathrm{T}}\mathbf{x} - wt)}, \tag{13}$$

where $\tilde{\mathbf{u}}$ is the Bloch function, t is the time, $\mathrm{i} = \sqrt{-1}$, and, for a two-dimensional system, $\mathbf{x} = (x, y)$ is the position and $\mathbf{k} = \left(k_x, k_y\right)$. Consider the unit cell represented in Fig. 1(a). The set of edge nodes belonging to the top and right edges (dashed lines in Fig. 1(a)) constitutes a redundant DOF as these nodes actually belong to neighboring unit cells. Hence, these sets of DOF are removed by linking them to the corresponding DOF belonging to the bottom and left edges (continuous lines in Fig. 1(a)). The equations representing the boundary conditions are collected in matrix form and inserted into the mass and stiffness matrices through a transformation matrix. Specific details on how these sets of DOF are defined, linked, and inserted into the Bloch transformation matrix are found in Ref. [40].

3. Unit-cell time-domain simulation

Time integration method. Eq. (10) is integrated in time using one of the several forms of Newmark's time-integration methods [46], yielding the computation of the displacements, velocities, and accelerations for increasing values of t. Following Newmark's family of methods, the discrete system of equations are

$$\mathbf{D}_{i+1} = \mathbf{D}_i + \Delta t \mathbf{V}_i + (\Delta t)^2 \left[\left(\frac{1}{2} - \beta\right)\mathbf{A}_i + \beta \mathbf{A}_{i+1}\right], \tag{14}$$

$$\mathbf{V}_{i+1} = \mathbf{V}_i + \Delta t \left[(1 - \gamma)\mathbf{A}_i + \gamma \mathbf{A}_{i+1}\right], \tag{15}$$

$$\mathbf{M}\mathbf{A}_{i+1} + \mathbf{K}\mathbf{D}_{i+1} = \mathbf{F}_{i+1}. \tag{16}$$

In these equations, $\mathbf{D}$, $\mathbf{V}$, and $\mathbf{A}$ denote displacement, velocity, and acceleration vectors, respectively. The time interval is denoted by Δt and i indicates the time step. The quantities β and γ are the Newmark parameters determining the specific type of Newmark scheme, which affects the accuracy and the stability of the numerical simulation. In this work, these parameters are chosen to be $\beta = 0, \gamma = 1/2$, providing an explicit central-difference Newmark scheme, which is computationally efficient and less demanding in its storage requirements compared to implicit methods. However, an explicit Newmark scheme is conditionally stable, thus the time interval is defined such that the Courant–Friedricks–Levy (CFL) lies at the stability limit

$$\Delta t = \frac{\Delta h^{\mathrm{e}}}{c_{\max}}, \tag{17}$$

where Δh^{e} is the element size and $c_{\max}$ is the highest phase velocity in any of the sub-media (or material types) considered in the model. For time intervals below the quantity specified in Eq. (17), some accuracy is compromised but stability is still guaranteed.

The procedure for solving for the elastodynamic wave propagation response using the selected Newmark scheme is done as follows. Given $\mathbf{K}$, $\mathbf{M}$, $\mathbf{F}$ and proper initial conditions for prescribed displacement, the following steps are carried out to compute the displacement, velocity and acceleration:

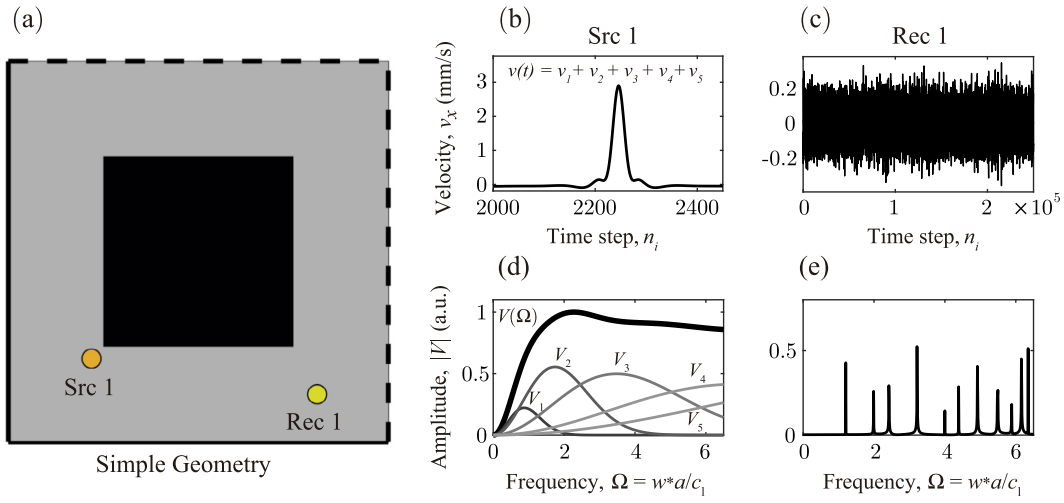

Fig. 1. Location and form of input and output signals used for the 2D time-domain simulations. (a) Unit cell having a simple geometry. (b), (c) Ricker wavelet used as a prescribed displacement excitation signal and recorded signal at a random point in the unit cell, respectively. (d), (e) Fourier transform of the above signals. The spectrum of each of the 5 Ricker wavelets used to build the excitation signal is also shown in (d).

1. Use Eq. (16) to obtain the acceleration vector at $t = 0$, i.e., $\mathbf{A}_i$. This is done by replacing the $i+1$ with i in this equation and using $\mathbf{D}_i$ as an initial condition. The force vector $\mathbf{F}$ is set to zero throughout the simulation.
2. Obtain the displacement vector for the first future time step, i.e., $\mathbf{D}_{i+1}$. This is done by applying Eq. (14) and using the displacement and velocity vectors at $t = 0$, i.e., $\mathbf{D}_i$ and $\mathbf{V}_i$, as initial conditions.
3. Use Eq. (15) to evaluate $\mathbf{V}_{i+1}$.
4. Use Eq. (16) to evaluate $\mathbf{A}_{i+1}$.
5. Advance in time and use Eqs. (14), (15), and (16) in this order to obtain the displacement, velocity and acceleration vectors, respectively, in the next time step.
6. Repeat the last step numerous times until the entire time range of interest is covered.

Transient excitation. A wide-band frequency signal is used to excite all the modes required to calculate the dispersion relation of the system up to the frequency limit where the FE discretization begins to introduce noticeable errors. A Ricker wavelet (also known as the Mexican hat signal) is applied as a prescribed displacement at a random point in the unit cell, as shown in Fig. 1(a), where a squared unit cell with a side length of $a = 1$ m is represented. The Ricker wavelet is the second derivative of a Gaussian function, defined as

$$u(t) = a^2\left(a^2t^2 - 1\right)e^{-\frac{a^2t^2}{2}}, \tag{18}$$

with $f_c = \frac{\sqrt{\pi}\cdot a}{2}$ defining the central frequency of the signal. The main advantage of this choice of signal is the absence of a zero-frequency component, which is susceptible to introducing numerical artifacts in the scheme and should be filtered out from the recorded displacement field if present [27]. On the other hand, the Ricker wavelet possesses a limited bandwidth around its central frequency, especially at low frequencies, which prevents the excitation of a sufficient number of modes of vibration. Therefore, we define 5 Ricker wavelets having central frequencies $f_{c,1} = 0.25 \times 10^3$ Hz, $f_{c,2} = 0.5 \times 10^3$ Hz, $f_{c,3} = 1 \times 10^3$ Hz, $f_{c,4} = 2 \times 10^3$ Hz, and $f_{c,5} = 4 \times 10^3$ Hz, (where $\Omega = 2\pi f_{c,i}a/c_l$ and c_i is the phase velocity the medium where the prescribed signal is applied) and consider their total displacement response in the time domain i.e., $u(t) = u_1 + u_2 + u_3 + u_4 + u_5$. This extends the total band width of the signal to cover the necessary frequency range for the target band-structure calculations (e.g., roughly the first 12 branches). The resulting combined signal is shown in Fig. 1(b) in the time-domain and in Fig. 1(d) in the frequency domain. Moreover, the frequency spectrum of each of the five signals used to obtain the total prescribed signal is also shown in Fig. 1(d), (where V_i denotes the amplitude of the response stemming from the application of the excitation with central frequency $f_{c,i}$).

Calculation of frequency band structure and bloch mode shapes. The procedure to obtain the band structure starts by setting up a value for the Bloch wave vector $\mathbf{k}$, which is inserted into the mass and stiffness matrices through the Bloch boundary transformation matrix (due to the dependence on the wave vector, the Bloch boundary transformation must be applied at each $\mathbf{k}$ point). Then, a transient excitation is applied at a random point within the unit cell for $t = 0$ as described above. As the time is incremented, Eqs. (14), (15) and (16) are used to solve for future displacements, velocities and accelerations at every node. A detector is randomly placed at one node in order to record the temporal signal for the displacement, as illustrated in Fig. 1(a). The time–history data is Fourier transformed into the frequency domain using the Fast Fourier Transform (FFT) method, obtaining a set of resonant modes as illustrated in Fig. 1(e). For a sufficiently long period of time, the error introduced by the assumption of periodicity in the recorded signals is minimized (see Section 5 for details). Each of the peaks of these resonant modes in the frequency domain corresponds to the eigenvalue of a vibrational mode for the given Bloch wave vector $\mathbf{k}$. The spanning of $\mathbf{k}$ along the IBZ allows for obtaining the resonant modes, and hence, the dispersion curves.

In addition to obtaining the band structure, the computation of Bloch mode shapes is also necessary to fully characterize the dispersion characteristics of the periodic medium. Unlike a standard eigenvalue problem, for which the eigenvalues and eigenvectors provide the band structure and Bloch mode shapes, respectively, the proposed time-domain technique allows for obtaining the eigenvalues only. However, the well-known experimental modal analysis procedure [47] may be utilized to compute the mode shapes from a set of frequency response functions (FRF) for the Bloch transformed unit cell. Moreover, the Modal Assurance Criterion (MAC) [48] may be employed in order to identify and solve degenerate modes at high-symmetry points by comparing Bloch mode shapes obtained from sources placed at two different points in the unit cell (see Fig. 1(a)). The computation of Bloch mode shapes requires the recording of the displacement field signals at every node in order to obtain the required FRFs. Hence, the number of detectors used is equal to the number of nodes in these calculations.

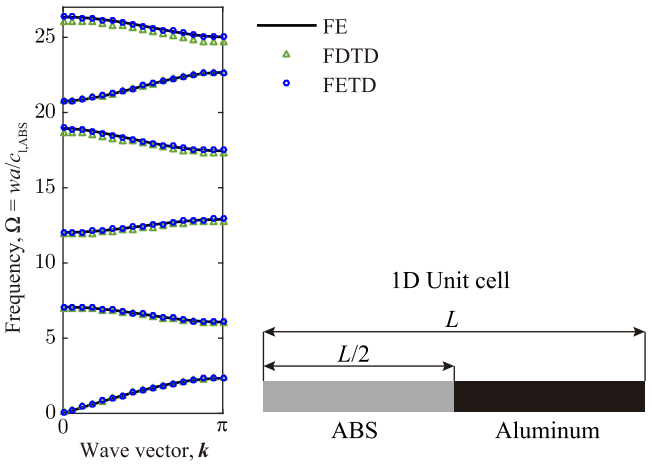

Fig. 2. Phononic band structure for longitudinal elastic waves in a 1D phononic crystal. An aluminum and ABS unit cell is considered, with a filling fraction $f_r = 0.5$. Black solid lines, green triangles, and blue dots correspond to FE, FDTD, and FETD results, respectively.

4. Numerical examples

The proposed FETD method is used to compute the band structure of 1D and 2D phononic crystals in this Section. Results are presented and compared to the solutions obtained by solving the corresponding standard eigenvalue problem by FE, selected as a reference method. An analogous FDTD method that also incorporates Bloch boundary conditions is implemented for comparison (see Appendix for a detailed description of discretization scheme and the approach followed for applying the Bloch boundary conditions). All examples considered are for unit cells composed of aluminum and an ABS polymer. The properties of these materials are: density $\rho = 2700$ kg/m^3, Young's modulus, $E = 70$ GPa, Poisson ratio, $\nu = 0.34$ for aluminum, and $\rho = 1050$ kg/m^3, $E = 2.3$ GPa and $\nu = 0.34$ for ABS.

1D phononic crystal. In the one-dimensional problem, we consider longitudinal wave propagation (axial modes) along a slender rod with a unit cell composed of two layers of equal length of ABS and aluminum with a filling fraction $f_r = 0.5$, as shown in the schematic diagram in Fig. 2. Bloch periodic boundary conditions are applied at the ends of the unit cell which allows us to represent a periodic rod of infinite length. Band-structure results are depicted in Fig. 2, showing calculations using FE (eigenvalue problem), FDTD and FETD. The unit cell in both the FE and FETD methods is discretized in space into $n_{el} = 256$ two-node elements, while for the FDTD method the grid is staggered and composed of $n = 256$ points for the stress and $n + 1$ points for the velocity. For the two time-domain methods, the time evolution is simulated over $n_{st} = 2^{20}$ (1,048,576) steps with a time interval $\Delta t = 5.4 \times 10^{-7}$ s, as stated in Eq. (17). As observed in Fig. 2, nearly identical eigenvalues are obtained using FE and FETD, and some discrepancies are found for the FDTD case. These differences are analyzed in detail in Section 5.

2D phononic crystal. Two different geometries comprising a square lattice are considered in the two-dimensional problem. Both geometries are composed of an ABS matrix and an aluminum inclusion placed at the center of the unit cell. The first geometry incorporates a simple square aluminum inclusion, denoted from now on as *simple geometry*, while the second geometry incorporates an inclusion with a complex shape, denoted as *complex geometry*. This complex shape, which is inspired by the helicoid–catenoid logo of the Phononics 20xx conference series [49], exhibits varying curvatures. Fig. 3 illustrates the meshes used for the simple and complex geometries. For the simple geometry, all the methods under evaluation (FE, FDTD, FETD) implement a structured and uniform grid; see Fig. 3(a), (b). The grid for FE-based methods is formed by $n = n_x \times n_y = 32^2$ elements where each element has two nodes in each direction (n_x and n_y define the number of elements in the x and y directions, respectively). The grid for FDTD is composed of $n_x \times n_y = 32^2$ points for normal stress, $= n_x + 1 \times n_y + 1 = 33^2$ for shear stress, and $n_x + 1 \times n_y$ and $n_x \times n_y + 1$ points for the x and y components of the velocity field. In this manner, the total number of nodal degrees of freedom is the same for all three methods, $N_{dof} = 2178$. After application of the Bloch boundary conditions, this number is reduced to $N_{dof} = 2048$, since the nodes lying at the top and right sides of the unit cell belong to neighboring unit cells and are condensed out. The complex geometry is designed to explore one of the main advantages of FE-based methods over FD methods, namely the use of unstructured grids. Fig. 3(c), (d) illustrate the two different approaches used to mesh a complex shape, an unstructured grid used for FE and FETD, which is precisely adapted to the shape of the inclusion, and a structured and uniform grid used for FDTD, where the geometry of the inclusion is described with much less accuracy. The total number of nodal degrees of freedom used for the FE-based methods, after application of Bloch boundary conditions, is $n_{dof} = 2560$. For the FDTD case, it is not possible to have the same exact number of degrees of freedom due to the different type of mesh used, although the number of points in the mesh is chosen so that the number of degrees of freedom after reduction due to periodicity is the closest possible value compared to that used for the FE-based models, $n_{dof} = 2520$. The **k**-space is discretized such that $l_k = 17$. Hence, a total of $n_k = 49$ **k**-points are evaluated to generate the elastic band structure along the main symmetry directions. For the time domain methods, the total number of steps is set to $n_{st} = 2^{18} = 262{,}144$ time steps, and the time interval is obtained by applying Eq. (17), resulting in a time interval $\Delta t = 1.57 \times 10^{-6}$ s for the simple geometry (the corresponding frequency resolution is $\Delta f = 1/(\Delta t n_{st}) = 2.4$ Hz). Different time intervals are set for the complex geometry due to the different type of meshes used. For FETD, the time interval for the complex geometry model is calculated considering the smallest element size, $\Delta t = 4.45 \times 10^{-7}$ ($\Delta f = 8.56$ Hz). The corresponding time interval for FDTD is set to $\Delta t = 2.88 \times 10^{-6}$ ($\Delta f = 1.32$ Hz).

Fig. 4 provides band structure results along the boundaries of the IBZ for the simple [(a) and (b)] and complex [(c) and (d)] geometries. For both geometries, consistent and lumped mass matrices are used for the finite-element-based methods, FE, FETD. Black (gray) solid lines illustrate FE results for consistent (lumped) mass matrices and blue (red) dots represent FETD results for consistent (lumped) mass matrices. Green triangles represent FDTD results. An excellent agreement is noted between the results obtained by the proposed FETD method and by solving the standard eigenvalue problem by FE, regardless of the geometry used. Noticeable differences are, however, observed in the results obtained using FDTD. While clear differences are found already using a simple geometry with the same type of mesh (Fig. 4(a), (b)), these are greatly increased for the complex geometry, as the structured mesh used in FDTD fails to properly capture the effects of the curved shape of the aluminum inclusion. A detailed analysis of the accuracy (in terms of the number of time steps), convergence, and computational efficiency for $\mathbf{k} = (\pi/2a, \pi/2a)$ is presented later in Section 5.

Bloch mode shapes. The periodic Bloch mode shapes ϕ_{td} computed with the time-domain algorithm are obtained from FRFs (akin to experimental modal analysis) and expanded to full size using a transformation operation [40]. A comparison of the Bloch mode shapes calculated using FE and FETD models with the same number

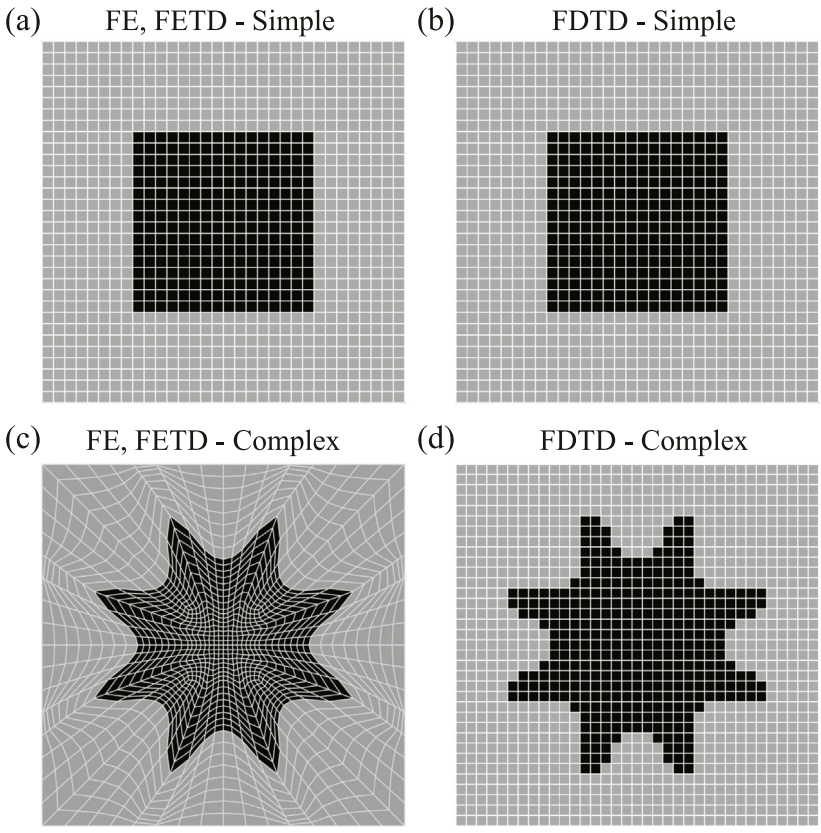

Fig. 3. Meshes used for the 2D numerical calculations using FE, FETD and FDTD. Structured and uniform meshes used to model the simple geometry using (a) FE, FETD and (b) FDTD. (c) Unstructured mesh generated using finite-elements to model the complex geometry. (d) Structured and uniform mesh to model the complex geometry using FDTD.

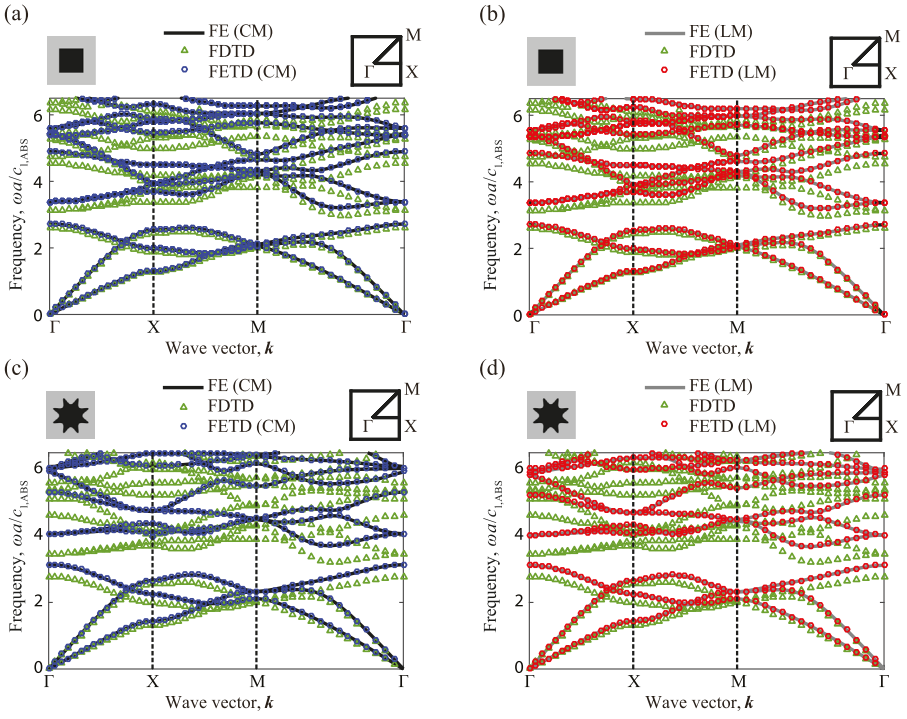

Fig. 4. Phononic band structure for longitudinal and shear-vertical elastic waves in 2D phononic crystals with the two different geometries, considering only wave vectors confined to the edge of the IBZ. Results are shown for FE and FETD based on consistent and lumped mass models. Results corresponding to the FDTD implementations are also shown. Black solid lines and blue/red dots correspond to FE and FETD, respectively; while green triangles correspond to the FDTD results. (For interpretation of the references to color in this figure legend, the reader is referred to the web version of this article.)

of degrees of freedom, for the 3rd branch at $\mathbf{k} = (\pi/2a, \pi/2a)$, is depicted in Fig. 5 for consistent and lumped mass matrices, showing the two geometries under examination. The structure of the mode shapes do not indicate clear differences between the two methods at a first glance. The Bloch mode-shape error is quantified by comparing the FETD mode shapes ϕ_{td} to the FE mode shapes ϕ_{fe}, and is defined as

$$e_{\text{m}} = 1 - \frac{\text{abs}\left[\phi_{\text{td}}{}'\phi_{\text{fe}}\right]}{|\phi_{\text{td}}|\,|\phi_{\text{fe}}|}, \tag{19}$$

where abs[·] denotes the complex modulus, and $|\cdot|$ denotes the vector 2-norm. The resulting error is $e_{\text{m,cm}} = 1.42 \cdot 10^{-4}$ and $e_{\text{m,lm}} = 4.66 \cdot 10^{-5}$ for the simple geometry case shown in Fig. 5(a), (b) and Fig. 5(e), (f) corresponding to the consistent and lumped mass models, respectively. It is also noted that the error is of the same order for the 10 first branches, and is below the following limits: $e_{m,cm} < 1.94 \cdot 10^{-4}$; $e_{m,lm} < 1.56 \cdot 10^{-4}$. The error in the mode shape calculations for the complex geometry is also very low, although it is slightly higher than the simple-geometry case; it is $e_{\text{m,cm}} = 7.16 \cdot 10^{-4}$ and $e_{\text{m,lm}} = 3.44 \cdot 10^{-4}$ for the 3rd branch at $\mathbf{k} = (\pi/2a, \pi/2a)$, and it is below the following limits for the first 10 branches: $e_{m,cm} < 3.38 \cdot 10^{-3}$; $e_{m,lm} < 1.98 \cdot 10^{-3}$.

5. FETD method performance

Accuracy. We evaluate the relative error as a function of the total number of steps n_{st} by comparing the predicted eigenvalues using FETD versus direct solution by FE for the simple and complex geometries. All the error results shown here are obtained using models having the same exact meshes presented in Fig. 3, and are calculated as follows:

$$e_{\text{st}} = \frac{f_{\text{td}} - f_{\text{fe}}}{f_{\text{fe}}}, \tag{20}$$

where f_{td}, f_{fe} are the computed eigenvalues for the 3$^{\text{rd}}$ branch at $\mathbf{k} = \pi/a$ (1D) or $\mathbf{k} = (\pi/2a, \pi/2a)$ (2D) for the time-domain methods, that is FDTD and FETD, and the direct FE method based on eigen analysis, respectively. The direct application of the FE method is based on a consistent mass model and is used as the reference case. The reference models have $N_{\text{dof}} = 512$ periodic DOF in 1D, and $N_{\text{dof}} = 32{,}768$, $N_{\text{dof}} = 40.960$ periodic DOF in 2D for the simple and complex geometries, respectively. Results shown in Fig. 6(a) are for the 1D problem. The error here converges to a minimum and a constant value as the number of steps is increased, falling quickly below 1% and being almost negligible for $n_{st} > 2^{20}$. In contrast, the finite-difference approach converges to a slightly larger error value of 1.5%. For the 2D problem, FETD results show a similar trend for both the consistent and lumped mass cases and both type of geometries; the error is maximum for small number of steps and is rapidly reduced as the recorded signals progress in time, being below 1% and 2% for the simple and complex geometries, respectively, as shown in Fig. 6(b), (c). Note that for a very low number of time steps, the assumption of periodicity in the recorded signals is not accurate, resulting in higher relative error in the eigenfrequency estimations when transforming the temporal signals into the frequency domain. The importance of the spatial discretization procedure arises when comparing the FDTD results between the simple and complex geometries, where the error is dramatically increased from an acceptable value of $\approx$3% for the simple geometry to a significant value of $\approx$10% for the complex geometry. This result clearly demonstrates how the proposed FETD method offers a much more precise way to handle complex geometries compared to other existent time domain methods for band structure calculations, such as FDTD. As stated previously, the frequency resolution Δf is inversely proportional to the product of the time interval and the total number of steps, resulting in a higher resolution (lower Δf) as the number of steps is increased. This is clearly observed in the sawtooth pattern of the error signals, where Δf is related to the difference between the local maxima and minima.

Convergence. The relative error in the band-structure calculations as a function of the number of DOF is calculated using the following expression:

$$e_{\text{dof}} = \frac{f_{N_{\text{dof,td}}} - f_{N_{\text{ref,fe}}}}{f_{N_{\text{ref,fe}}}}, \tag{21}$$

where $f_{N_{\text{dof,td}}}$ denotes an eigenvalue computed in the time domain for a given number of DOF and $f_{N_{\text{ref,fe}}}$ denotes an eigenvalue computed for the reference FE model having the same number of degrees of freedom as the reference models considered in Fig. 6. Note that since the reference case is taken as the direct eigenvalue solution for the finest resolved model under analysis, the FE error will eventually reach a value of $e_{dof} = 0$. The total number of time steps used for these calculations for the time-domain methods is $n_{st} = 262{,}144$. Error results are depicted in Fig. 7(a)–(c) for the 4th branch at wave vector $\mathbf{k} = (\pi/2a, \pi/2a)$. Results show, as a general trend, a much slower convergence for the FDTD method regardless of the dimensionality and geometry considered, and a very similar convergence between FE and FETD methods for both consistent and mass matrices. For the 1D case, the error is reduced below 1% for a moderate number of DOF ($N_{\text{dof}} = 32$) for FE-based methods, while for FDTD, 256 DOFs are needed to get an error below this value. In 2D, convergence is quite fast for all the finite-element methods for a simple geometry, with an error below 2.5% even for the smallest model size; while relatively finely resolved models ($N_{\text{dof}} = 8192$) are needed using FDTD to get acceptable errors, i.e., below 2%. Finally, the results for the complex geometry show a general increase in the error for all methods, especially for small-size models, as expected. However, FE and FETD error values are much lower than FDTD. This is attributed mostly to the geometry conforming mesh used, which describes the geometric complexity in the material distribution with much more accuracy than the uniform mesh used for FDTD. Furthermore, we observe that FE-based methods exhibit higher accuracy than FDTD even at a very high number of DOF (e.g., see the differences between FETD and FDTD error values for $N_{\text{dof}} = 40{,}960$ at the far right end of Fig. 7c).

Computational efficiency. The computation time of the proposed FETD method is dominated by the acceleration calculation in Eq. (16), which has to be done n_{st} times for each $\mathbf{k}$ point. The computation time of the FE method is dominated by the eigenvalue calculation. Both the FE-based and the FD-based methods produce sparse matrix structures. For large model sizes, it is critical to take advantage of this sparsity to reduce memory requirements and computational complexity. Both the model creation and the numerical simulations in this paper are carried out using the commercial software Matlab [50].

The computation time (depicted in logarithmic scale) versus N_{dof} is observed in Fig. 8 for the (a) 1D model, and (b) 2D simple-geometry model. Note that the computational complexity is independent of the type of mesh used; hence the calculation in 2D is restricted to the simple geometry. Every set of data obtained by the different methods used in this work are fitted to obtain a rough estimation of the numerical complexity. A function of the form $\bar{y} = a\bar{x}^b$ is used, were $\bar{y}$ denotes the computational time and $\bar{x}$ represents the number of DOF. Results for the fittings are shown in Table 1. Results for both the 1D and 2D cases indicate a higher computation time for the time-domain algorithms compared to FE. However, linear complexity is evident for all the finite-elements methods (FE, FETD). This is expected due to the sparse representation of the mass and stiffness matrices, with very small

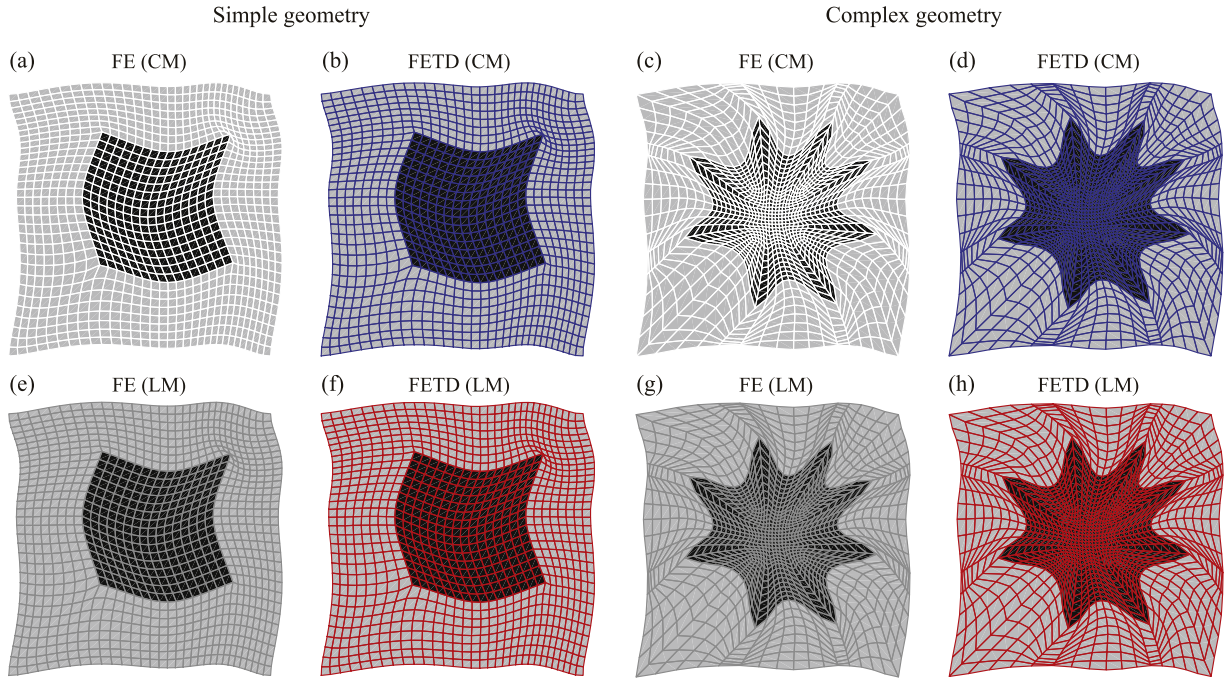

Fig. 5. Calculated mode shapes for the 3rd branch at $\mathbf{k} = (\pi/2a, \pi/2a)$ for the simple and complex geometries of 2D phononic crystals. (a), (e) illustrate mode shapes extracted from FE calculations for a simple geometry using consistent and lumped masses, respectively. (b), (f) represent mode shapes calculated using the FETD method for the simple geometry and considering consistent and lumped mass matrices, respectively. Mode shapes calculated for the complex geometry are shown in (c), (g) using FE and consistent and lumped masses, respectively, and in (d), (h) using FETD and consistent and lumped masses, respectively.

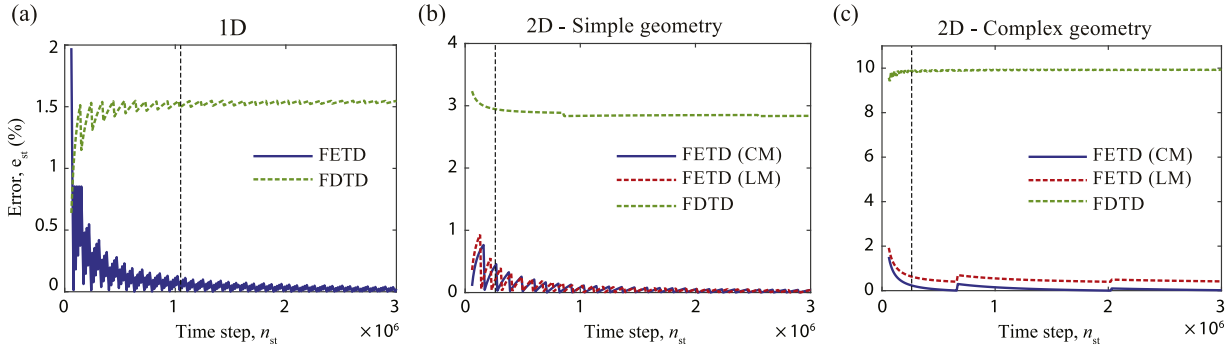

Fig. 6. Time-domain methods error in frequency as a function of number of time steps for (a) 1D, (b) 2D simple geometry, and (c) 2D complex geometry. Results are shown for the 3rd branch and wave vector $\mathbf{k} = \pi/a$ in 1D and $\mathbf{k} = (\pi/2a, \pi/2a)$ in 2D. Vertical dashed black lines indicate the number of time steps used for all other calculations presented in this work: $n_{st,1D} = 1{,}048{,}576$ and $n_{st,2D} = 262{,}144$. The reference method is high-resolution FE eigenvalue analysis using consistent mass matrices.

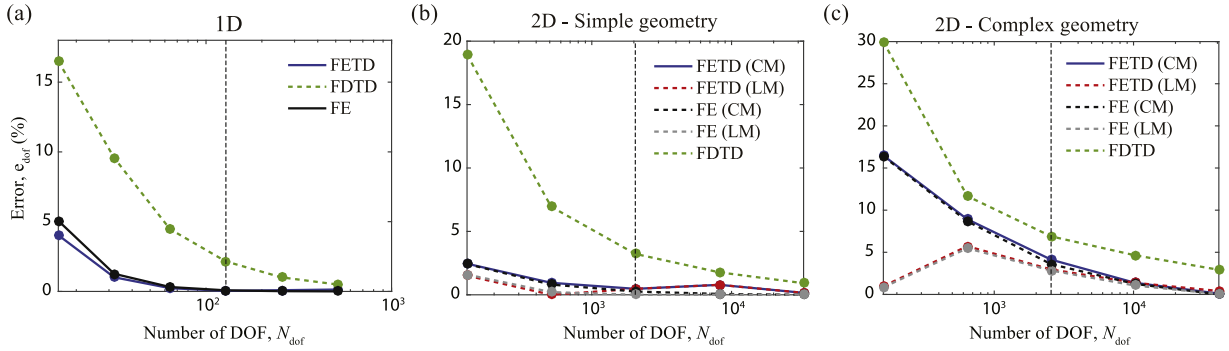

Fig. 7. Frequency error estimation as a function of number of DOF for (a) 1D, $\mathbf{k} = \pi/a$, (b) 2D simple geometry, $\mathbf{k} = (\pi/2a, \pi/2a)$, and (c) 2D complex geometry, $\mathbf{k} = (\pi/2a, \pi/2a)$. Results are shown for the 4th branch. Vertical dashed black lines in the three subfigures mark the number of DOF used in Fig. 2 and Figs. 4 and 5, which are $n_{dof,1D} = 256$, and $n_{dof,2D} = 2048$ for the simple geometry and $n_{dof,2D} = 2560$ for the complex geometry. The reference method is high-resolution FE eigenvalue analysis using consistent mass matrices.

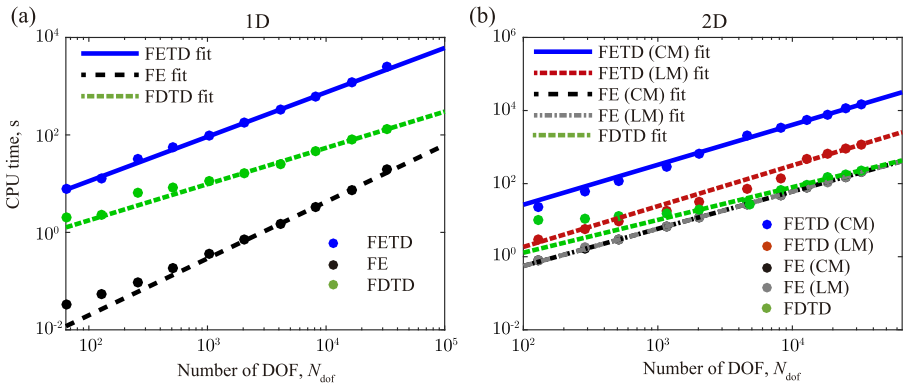

Fig. 8. Computation time as a function of number of degrees of freedom for (a), 1D, $\mathbf{k} = \pi/a$, and (b), 2D, $\mathbf{k} = (\pi/2a, \pi/2a)$. Circles represent the computation time results obtained directly from numerical simulations and lines represent curve fits of this data using the expression $\bar{y} = a\bar{x}^b$. Note that the number of DOF used for the calculations presented in Figs. 2 and 3 are $N_{\text{dof,1D}} = 256$, $N_{\text{dof,2D}} = 2048$, respectively.

Table 1
Table summarizing computational complexity of proposed FETD method versus other techniques.

	Method	$\bar{y} = a\bar{x}^b$	Complexity
1D	FETD	$1.7 \times 10^{-1}(N_{dof})^{0.91}$	$\mathcal{O}(n^{0.91})$
	FE	$9.3 \times 10^{-5}(N_{dof})^{1.16}$	$\mathcal{O}(n^{1.16})$
	FDTD	$5.7 \times 10^{-2}(N_{dof})^{0.74}$	$\mathcal{O}(n^{0.74})$
2D	FETD (CM)	$1.7 \times 10^{-1}(N_{dof})^{1.09}$	$\mathcal{O}(n^{1.09})$
	FETD (LM)	$1.1 \times 10^{-2}(N_{dof})^{1.12}$	$\mathcal{O}(n^{1.12})$
	FE (CM)	$5.1 \times 10^{-3}(N_{dof})^{1.02}$	$\mathcal{O}(n^{1.02})$
	FE (LM)	$5.1 \times 10^{-3}(N_{dof})^{1.02}$	$\mathcal{O}(n^{1.02})$
	FDTD	$2.1 \times 10^{-2}(N_{dof})^{0.90}$	$\mathcal{O}(n^{0.90})$

differences in the exponents probably due to a small uncertainty in the evaluation of the computation time. The FDTD method is observed to exhibit the lowest complexity among all methods considered. Upon comparing Fig. 7c for convergence and Fig. 8b for computation time, it is evident that a problem-specific error versus computation time analysis is needed to assess which of the FETD and FDTD methods is faster for a given error threshold— is it FETD with a smaller N_{dof} but good convergence or is it FDTD with a larger N_{dof} but good efficiency.

6. Conclusions

A new method for elastic band-structure calculations based on finite-element spatial discretization and time-domain simulations is proposed and analyzed in this paper. This method, which is more generally a methodology with possible variations in implementation approaches, is denoted the FETD method for elastic band-structure calculations. The method incorporates Bloch boundary conditions that enable a reduction of the domain to a unit cell, in contrast to other time-domain methods where a certain number of unit cells is considered in the computations [25]. The domain is discretized in space by finite elements and in time using an explicit Newmark time-stepping scheme. The frequency band structure and mode shapes are calculated and compared to results obtained by the Bloch-reduced FDTD method, which is a corresponding technique, demonstrating superior accuracy and convergence performance of the new method. An advantage of FE-based methods is that FE discretization easily handles complex geometries and generally outperforms finite-difference methods, as demonstrated using a unit cell incorporating a complex-shaped inclusion where it was shown that the proposed FETD method strongly gives better performance in both the accuracy (Fig. 6) and the convergence (Fig. 7). The computational efficiency of the new method, while lower than FDTD, does exhibit linear complexity. The FETD and FDTD methods enable band-structure calculation for problems where it is not possible to formulate an eigenvalue problem using the direct FE or FD methods, such as unit cells with a dynamically flowing fluid for example.

Future improvements may be implemented to increase the computational efficiency while maintaining the same accuracy. For example, the definition of a pseudoperiodic initial field distribution, which is consistent with the periodicity enforced at the boundaries of the unit cell, can reduce considerably the total number of time steps needed to compute the band structure (as reported in Ref. [30] for FDTD elastic band-structure calculations). Furthermore, the length of the time–history data may be dramatically reduced by considering an alternative to a standard Fourier transform for the transformation to the frequency domain. This may be done using a post-processing method called the high-resolution spectral estimation method [51].

Acknowledgments

A.C. is grateful for the support of Programa de Ayudas de Investigación y Desarrollo (PAID) and Programa de Movilidad e Internacionalización Académica (PMIA-2013) of the UPV. This research was partially funded by the funded by the Ministerio de Economia e Innovacion (MINECO), Spain through project FIS2015-65998-C2-2-P, and partially funded by the National Science Foundation (NSF), USA through grant number 1538596. The authors acknowledge Dr. Noé Jimenez for fruitful discussions.

Appendix. Finite-difference time-domain model

We describe here the discretization and modeling details of the FDTD method used in this work. We consider wave propagation along isotropic materials in the linear regime and without losses. The dynamics of an inhomogeneous elastic solid under these conditions in two dimensions is expressed as follows based on a Cartesian coordinate system:

$$\rho\dot{\mathbf{v}} = \nabla \cdot \boldsymbol{\sigma}, \tag{A.1}$$

$$\dot{\boldsymbol{\sigma}} = \lambda\bar{\mathbf{I}}\nabla\mathbf{v} + \mu(\nabla\mathbf{v} + \mathbf{v}\nabla), \tag{A.2}$$

where $\mathbf{v} = (v_x, v_y)$ is a vector representing the velocity field, $\boldsymbol{\sigma} = (\sigma_{xx}, \sigma_{yy}, \sigma_{xy}, \sigma_{yx})$ is a matrix representing the stress field and λ, μ are the Lamé parameters.

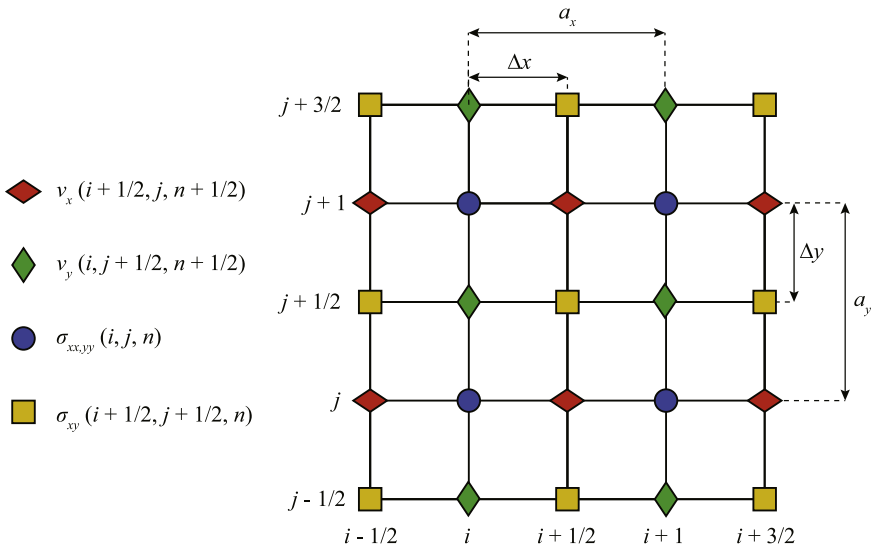

Fig. A.1. Schematic representation of the adopted FDTD scheme.

Discretization

The discretization of the velocity, normal stress, and shear stress fields shown in Eqs. (A.1) and (A.2) is performed using a time interval Δt, and space intervals Δx and Δy, with $\Delta x = \Delta y$. Partial derivatives are substituted by their central finite-difference approximations. The scheme staggers the velocity fields in time and space with respect to the stress fields. Furthermore, the shear stress components are staggered in space with respect to the normal stress components. Thus, the spatial distribution of the fields result in the spatial distribution shown in Fig. A.1. Note that (i, j) represents the position index of the x, y directions in the 2D grid, and n denotes the time step index.

The explicit expressions of the discretized versions of Eqs. (A.1) and (A.2) are as follows:

$$\rho\frac{v_x^{n+\frac{1}{2}}\left(i+\frac{1}{2},j\right)-v_x^{n-\frac{1}{2}}\left(i+\frac{1}{2},j\right)}{\Delta t}=\frac{\sigma_{xx}^{n}\left(i+1,j\right)-\sigma_{xx}^{n}\left(i,j\right)}{\Delta x}+\frac{\sigma_{xy}^{n}\left(i+\frac{1}{2},j+\frac{1}{2}\right)-\sigma_{xy}^{n}\left(i+\frac{1}{2},j-\frac{1}{2}\right)}{\Delta y}, \tag{A.3}$$

$$\rho\frac{v_y^{n+\frac{1}{2}}\left(i,j+\frac{1}{2}\right)-v_y^{n-\frac{1}{2}}\left(i,j+\frac{1}{2}\right)}{\Delta t}=\frac{\sigma_{yy}^{n}\left(i,j+1\right)-\sigma_{yy}^{n}\left(i,j\right)}{\Delta y}+\frac{\sigma_{xy}^{n}\left(i+\frac{1}{2},j+\frac{1}{2}\right)-\sigma_{xy}^{n}\left(i-\frac{1}{2},j+\frac{1}{2}\right)}{\Delta x}, \tag{A.4}$$

$$\frac{\sigma_{xx}^{n+1}\left(i,j\right)-\sigma_{xx}^{n}\left(i,j\right)}{\Delta t}=(\lambda+2\mu)\frac{v_x^{n+\frac{1}{2}}\left(i+\frac{1}{2},j\right)-v_x^{n+\frac{1}{2}}\left(i-\frac{1}{2},j\right)}{\Delta x}+\lambda\frac{v_y^{n+\frac{1}{2}}\left(i,j+\frac{1}{2}\right)-v_y^{n+\frac{1}{2}}\left(i,j-\frac{1}{2}\right)}{\Delta y}, \tag{A.5}$$

$$\frac{\sigma_{yy}^{n+1}\left(i,j\right)-\sigma_{yy}^{n}\left(i,j\right)}{\Delta t}=(\lambda+2\mu)\frac{v_y^{n+\frac{1}{2}}\left(i,j+\frac{1}{2}\right)-v_y^{n+\frac{1}{2}}\left(i,j-\frac{1}{2}\right)}{\Delta y}+\lambda\frac{v_x^{n+\frac{1}{2}}\left(i+\frac{1}{2},j\right)-v_x^{n+\frac{1}{2}}\left(i-\frac{1}{2},j\right)}{\Delta x}, \tag{A.6}$$

$$\frac{\sigma_{xy}^{n+1}\left(i+\frac{1}{2},j+\frac{1}{2}\right)-\sigma_{xy}^{n}\left(i+\frac{1}{2},j+\frac{1}{2}\right)}{\Delta t}=\cdots\mu\left(\frac{v_x^{n+\frac{1}{2}}\left(i+\frac{1}{2},j+1\right)-v_x^{n+\frac{1}{2}}\left(i+\frac{1}{2},j\right)}{\Delta y}+\frac{v_y^{n+\frac{1}{2}}\left(i+1,j+\frac{1}{2}\right)-v_y^{n+\frac{1}{2}}\left(i,j+\frac{1}{2}\right)}{\Delta x}\right), \tag{A.7}$$

where Eqs. (A.3) and (A.4) represent the velocity field in the x and y directions, respectively, Eqs. (A.5) and (A.6) represent the normal stress field in the x and y directions, respectively, and Eq. (A.7) represents the shear stress.

Boundary conditions

Similar to the FE and FETD methods, Bloch boundary conditions are used in the FDTD method. However, some differences in the their implementation are to be considered. In FDTD, Bloch boundary conditions are applied for both the velocity field

$$\mathbf{v}\left(\mathbf{x},\mathbf{k};t\right)=\tilde{\mathbf{v}}\left(\mathbf{x},\mathbf{k}\right)e^{\mathrm{i}(\mathbf{k}^{\mathrm{T}}\mathbf{x}-wt)}, \tag{A.8}$$

and the stress field

$$\boldsymbol{\sigma}\left(\mathbf{x},\mathbf{k};t\right)=\tilde{\boldsymbol{\sigma}}\left(\mathbf{x},\mathbf{k}\right)e^{\mathrm{i}(\mathbf{k}^{\mathrm{T}}\mathbf{x}-wt)}, \tag{A.9}$$

where the notation convention used in Eq. (13) is followed. The discretized version of these boundary conditions is as follows:

Normal to the x axis:

$$v_x^{n+\frac{1}{2}}\left(-\frac{1}{2},j\right)=e^{-\mathrm{i}k_x a_x}v_x^{n+\frac{1}{2}}\left(a_x-\frac{1}{2},j\right) \tag{A.10}$$

$$v_x^{n+\frac{1}{2}}\left(a_x+\frac{1}{2},j\right)=e^{\mathrm{i}k_x a_x}v_x^{n+\frac{1}{2}}\left(\frac{1}{2},j\right) \tag{A.11}$$

$$v_y^{n+\frac{1}{2}}\left(0,j-\frac{1}{2}\right)=e^{-\mathrm{i}k_x a_x}v_y^{n+\frac{1}{2}}\left(a_x,j-\frac{1}{2}\right) \tag{A.12}$$

$$v_y^{n+\frac{1}{2}}\left(a_x,j-\frac{1}{2}\right)=e^{\mathrm{i}k_x a_x}v_y^{n+\frac{1}{2}}\left(0,j-\frac{1}{2}\right) \tag{A.13}$$

$$\sigma_{xx,yy}^{n}\left(0,j\right)=e^{-\mathrm{i}k_x a_x}\sigma_{xx,yy}^{n}\left(a_x,j\right) \tag{A.14}$$

$$\sigma_{xx,yy}^{n}\left(a_x,j\right)=e^{\mathrm{i}k_x a_x}\sigma_{xx,yy}^{n}\left(0,j\right) \tag{A.15}$$

$$\sigma_{xy}^{n}\left(-\frac{1}{2},j-\frac{1}{2}\right)=e^{-\mathrm{i}k_x a_x}\sigma_{xy}^{n}\left(a_x-\frac{1}{2},j-\frac{1}{2}\right) \tag{A.16}$$

$$\sigma_{xy}^{n}\left(a_x+\frac{1}{2},j-\frac{1}{2}\right)=e^{ik_x a_x}\sigma_{xy}^{n}\left(\frac{1}{2},j-\frac{1}{2}\right) \tag{A.17}$$

Normal to the y axis:

$$v_x^{n+\frac{1}{2}}\left(i-\frac{1}{2},0\right)=e^{-ik_y a_y}v_x^{n+\frac{1}{2}}\left(i-\frac{1}{2},a_y\right) \tag{A.18}$$

$$v_x^{n+\frac{1}{2}}\left(i-\frac{1}{2},a_y\right)=e^{ik_y a_y}v_x^{n+\frac{1}{2}}\left(i-\frac{1}{2},0\right) \tag{A.19}$$

$$v_y^{n+\frac{1}{2}}\left(i,-\frac{1}{2}\right)=e^{-ik_y a_y}v_y^{n+\frac{1}{2}}\left(i,a_y-\frac{1}{2}\right) \tag{A.20}$$

$$v_y^{n+\frac{1}{2}}\left(i,a_y+\frac{1}{2}\right)=e^{ik_y a_y}v_y^{n+\frac{1}{2}}\left(i,\frac{1}{2}\right) \tag{A.21}$$

$$\sigma_{xx,yy}^{n}(i,0)=e^{-ik_y a_y}\sigma_{xx,yy}^{n}\left(i,a_y\right) \tag{A.22}$$

$$\sigma_{xx,yy}^{n}\left(i,a_y\right)=e^{ik_y x a_y}\sigma_{xx,yy}^{n}(i,0) \tag{A.23}$$

$$\sigma_{xy}^{n}\left(i-\frac{1}{2},-\frac{1}{2}\right)=e^{-ik_y a_y}\sigma_{xy}^{n}\left(i-\frac{1}{2},a_y-\frac{1}{2}\right) \tag{A.24}$$

$$\sigma_{xy}^{n}\left(i-\frac{1}{2},a_y+\frac{1}{2}\right)=e^{ik_y a_y}\sigma_{xy}^{n}\left(i-\frac{1}{2},\frac{1}{2}\right) \tag{A.25}$$

Special attention must be given to the implementation of these boundary conditions. The discretized version shown above clearly shows how these fields are staggered in space and time. However, it is not straightforward to consider that since stress and velocity fields are staggered in time, the application of these boundary conditions has to be performed immediately after each of the fields are updated. Thus, if the choice is to first solve Eqs. (A.5), (A.6), and (A.7), then the boundary conditions corresponding to the stress should be applied right after and always before updating the velocity fields, Eqs. (A.3) and (A.4). Once the velocity fields are updated, the corresponding boundary conditions have to be applied.

References

[1] S. John, Phys. Rev. Lett. 58 (23) (1987) 2486.
[2] E. Yablonovitch, Phys. Rev. Lett. 58 (20) (1987) 2059.
[3] M. Sigalas, E.N. Economou, J. Sound Vib. 158 (2) (1992) 377–382.
[4] M.S. Kushwaha, P. Halevi, L. Dobrzynski, B. Djafari-Rouhani, Phys. Rev. Lett. 71 (13) (1993) 2022.
[5] F. Bloch, Z. Phys. 52 (7–8) (1928) 555–600.
[6] C. Kittel, D.F. Holcomb, Amer. J. Phys. 35 (6) (1967) 547–548.
[7] K.M. Ho, C.T. Chan, C.M. Soukoulis, Phys. Rev. Lett. 65 (25) (1990) 3152.
[8] R.D. Meade, A.M. Rappe, K.D. Brommer, J.D. Joannopoulos, O.L. Alerhand, Phys. Rev. B 48 (11) (1993) 8434.
[9] S. Johnson, J. Joannopoulos, Opt. Express 8 (3) (2001) 173–190.
[10] V. Laude, Y. Achaoui, S. Benchabane, A. Khelif, Phys. Rev. B 80 (2009) 092301.
[11] V. Romero-García, J.V. Sánchez-Pérez, L.M. García-Raffi, J. Appl. Phys. 108 (2010) 044907.
[12] M. Sigalas, E.N. Economou, Solid State Commun. 86 (3) (1993) 141–143.
[13] J.B. Pendry, A. MacKinnon, Phys. Rev. Lett. 69 (19) (1992) 2772.
[14] K.M. Leung, Y. Qiu, Phys. Rev. B 48 (11) (1993) 7767.
[15] X. Wang, X.-G. Zhang, Q.-L. Yu, B.N. Harmon, Phys. Rev. B 47 (8) (1993) 4161.
[16] M. Kafesaki, E.N. Economou, Phys. Rev. B 60 (17) (1999) 11993.
[17] M. Kafesaki, R.S. Penciu, E.N. Economou, Phys. Rev. Lett. 84 (26) (2000) 6050.
[18] Z.-Y. Liu, C.T. Chan, P. Sheng, A.L. Goertzen, J.H. Page, Phys. Rev. B 62 (4) (2000) 2446.
[19] W. Axmann, P. Kuchment, J. Comput. Phys. 150 (2) (1999) 468–481.
[20] D.C. Dobson, J. Comput. Phys. 149 (2) (1999) 363–376.
[21] J.E. Pask, B.M. Klein, P.A. Sterne, C.Y. Fong, Comput. Phys. Comm. 135 (1) (2001) 1–34.
[22] M.I. Hussein, Proc. R. Soc. Lond. Ser. A Math. Phys. Eng. Sci. 465 (2109) (2009) 2825–2848.
[23] W.H. Yang, E.H. Lee, ASME J. Appl. Math. 41 (2) (1974) 429–433.
[24] H.Y.D. Yang, IEEE Trans. Microw. Theory Tech. 44 (12) (1996) 2688–2695.
[25] D. Garcia-Pablos, M. Sigalas, F.R. Montero de Espinosa, M. Torres, M. Kafesaki, N. Garcia, Phys. Rev. Lett. 84 (2000) 4349–4352.
[26] C.T. Chan, Q.L. Yu, K.M. Ho, Phys. Rev. B 51 (23) (1995) 16635–16642.
[27] A.J. Ward, J.B. Pendry, Phys. Rev. B 58 (11) (1998) 7252.
[28] M. Qiu, S. He, J. Appl. Phys. 87 (12) (2000) 8268–8275.
[29] Y. Tanaka, Y. Tomoyasu, Shin-ichiro Tamura, Phys. Rev. B 62 (11) (2000) 7387.
[30] Y. Cao, Z. Hou, Y. Liu, Solid state commun. 132 (8) (2004) 539–543.
[31] P.-F. Hsieh, T.-T. Wu, J.-H. Sun, IEEE Trans. Ultrason. Ferroelectr. Freq. Control 53 (1) (2006) 148–158.
[32] S. Jun, Y.-S. Cho, S. Im, Opt. Express 11 (6) (2003) 541–551.
[33] E. Moreno, D. Erni, C. Hafner, Phys. Rev. B 65 (15) (2002) 155120.
[34] X. Checoury, J.-M. Lourtioz, Opt. Commun. 259 (1) (2006) 360–365.
[35] Z.-Z. Yan, Y.-S. Wang, Phys. Rev. B 74 (22) (2006) 224303.
[36] P.-J. Chiang, C.-P. Yu, H.-C. Chang, Phys. Rev. E 75 (2) (2007) 026703.
[37] K. Busch, G. von Freymann, S. Linden, S.F. Mingaleev, L. Tkeshelashvili, M. Wegener, Phys. Rep. 444 (3) (2007) 101–202.
[38] M.I. Hussein, M.J. Leamy, M. Ruzzene, Appl. Mech. Rev. 66 (4) (2014) 040802.
[39] L. Brillouin, Wave propagation in periodic structures, Dover, New York, 1946.
[40] D. Krattiger, M.I. Hussein, Phys. Rev. E 90 (6) (2014) 063306.
[41] W.M. Robertson, J.F. Rudy III, J. Acoust. Soc. Am. 104 (2) (1998) 694–699.
[42] C. Rubio, D. Caballero, J.V. Sanchez-Perez, R. Martinez-Sala, J. Sanchez-Dehesa, F. Meseguer, F. Cervera, J. Lightwave Technol. 17 (11) (1999) 2202.
[43] F.L. Teixeira, IEEE Trans. Antennas Propag. 56 (8) (2008) 2150–2166.
[44] T.J.R. Hughes, The Finite Element Method, Prentice-Hall, New Jersey, 1987.
[45] E. Hinton, T. Rock, O.C. Zienkiewicz, Earthq. Eng. Struct. Dyn. 4 (3) (1976) 245–249.
[46] N.N. Newmark, ASCE J. Eng. Mech. 85 (1959) 67–94.
[47] D.J. Ewins, Modal Testing: Theory, Practice and Application, Research Studies Press, Hertfordshire, 2000.
[48] R.J. Allemang, Sound Vib. 37 (8) (2003) 14–23.
[49] M.I. Hussein, I. El-Kady, Preface to Special Topic: Selected Articles From Phononics 2011: The First International Conference on Phononic Crystals, Metamaterials and Optomechanics, 29 May–2 2011, Santa Fe, New Mexico, USA, in: AIP Advances, vol. 1, 2011, pp. 041301.
[50] MATLAB, The MathWorks, Inc., Natick, Massachusetts, United States.
[51] X.-X. Su, Y.-S. Wang, Proceedings of the 2ND International Symposium on Computational Mechanics and the 12th International Conference on the Enhancement and Promotion of Computational Methods in Engineering and Science, Vol. 1233, No. 1, AIP Publishing, 2010.